



Modeling of RDX/GAP/BTTN pseudo-propellant combustion

Jae-Kun Yoon, Piyush Thakre, Vigor Yang*

Department of Mechanical and Nuclear Engineering, The Pennsylvania State University, 104 Research Building East, University Park, PA 16802, USA

Received 7 March 2005; received in revised form 11 October 2005; accepted 12 October 2005

Available online 21 November 2005

Abstract

A comprehensive numerical analysis has been developed to predict the burning characteristics and detailed combustion wave structure of RDX/GAP/BTTN pseudo-propellant over a broad range of pressures. The present work extends an existing model for the steady-state combustion of RDX/GAP pseudo-propellant to include the salient features of BTTN, a commonly used plasticizer for practical solid propellants. The entire combustion zone is divided into the solid-phase, subsurface multiphase, and gas-phase regions. In the solid-phase region, the constituent ingredients are physically linked together and heated by conduction. Five global decomposition reactions, as well as subsequent reactions of RDX, GAP, and BTTN, are considered in the near-surface multiphase region. The overall gas-phase kinetics considers 72 species and 429 reactions in describing the heat-release mechanism. Good agreement is obtained with measured burning rates in the pressure range of 1–100 atm. The propellant surface temperature matches closely with the measured value and depends strongly on the RDX evaporation. The burning rate of RDX/GAP/BTTN is in general higher than that of RDX/GAP, a phenomenon that may be attributed to the stoichiometrically balanced nature of BTTN.

© 2005 The Combustion Institute. Published by Elsevier Inc. All rights reserved.

Keywords: Solid propellant combustion; RDX; GAP; BTTN

1. Introduction

In the recent past, experimental diagnostics [1,2] and theoretical analyses [3–10] have helped achieve major advances in the study of the combustion-wave structures and burning characteristics of nitramine monopropellants, such as cyclotrimethylenetrinitramine (RDX) and cyclotetramethylenetetranitramine (HMX), over a broad range of operating conditions. Both self-sustained combustion and laser-assisted

combustion [3–9], as well as ignition transients [10], have been treated in detail. Extensive experimental studies [11–17] and modeling efforts [18] have also been applied to investigate the combustion of glycidyl azide polymer (GAP). Still more recently, detailed modeling of RDX/GAP and HMX/GAP pseudo-propellant combustion was carried out by Liau and co-workers [19,20], while the experimental studies were performed by Litzinger et al. [21]. A comprehensive summary of the latest developments is covered in the volume compiled by Yang et al. [22].

So far, only monopropellants and pseudo-propellants containing binary oxidizer and fuel mixtures

* Corresponding author. Fax: +1 (814) 865 3389.
E-mail address: vigor@psu.edu (V. Yang).

Nomenclature

A	cross-sectional area of propellant sample	V_i	diffusion velocity of species i
A_g	fractional cross-sectional area consisting of gas bubbles in two-phase region	\bar{v}_n	average normal velocity component of vapor molecule
A_j	preexponential factor for rate constant in reaction j	W_i	molecular weight of species i
A_s	liquid–gas interface area per unit volume	\dot{w}_i	mass production rate of species i
a	preexponential factor in burning-rate law	\dot{w}_{R_j}	mass production rate of reaction j
B_j	temperature exponent for rate constant in reaction j	X_i	molar fraction of species i
C_i	molar concentration of species i	x	spatial coordinate
c_{p_i}	constant-pressure specific heat of species i	Y_i	mass fraction of species i
E_j	activation energy for reaction j	<i>Greek symbols</i>	
e	internal energy	ϕ	void fraction
H_v	enthalpy of vaporization	ρ	density
h	enthalpy	λ	thermal conductivity
h_c	heat transfer coefficient	$\dot{\omega}$	molar production rate
h_i	static enthalpy of species i	<i>Subscripts</i>	
$h_{f_i}^\circ$	standard heat of formation of species i	0^+	gas-phase side of propellant surface
k_j	rate constant for reaction j	0^-	condensed-phase side of propellant surface
\dot{m}''	mass flux	c	condensed phase
N	total number of species	$c-g$	from condensed to gas phase
n	pressure exponent	$cond$	condensation
N_R	total number of reactions	eq	equilibrium condition
p	pressure	$evap$	evaporation
p_0	preexponential factor for vapor pressure in Arrhenius form	f	mass-averaged quantity in subsurface foam layer
r_b	propellant burning rate	g	gas phase
R_u	universal gas constant	i	preconditioned state
T	temperature	l	liquid phase
s	sticking coefficient	s	propellant surface or solid phase
t	time	v	vapor
u	bulk velocity		

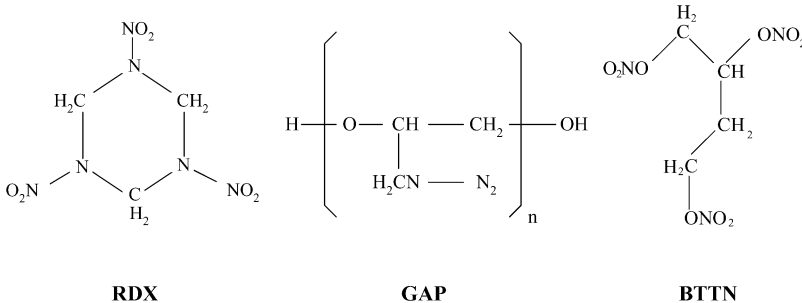


Fig. 1. Molecular structures of RDX, GAP, and BTTN.

have been modeled. The effects of plasticizer, curing agent, and other ingredients on propellant combustion characteristics have not been considered. As a step toward the ultimate goal of modeling the behavior of a practical solid propellant, the present work extends

our previous analysis of RDX/GAP [19] to include 1,2,4-butane triol trinitrate (BTTN), a commonly used plasticizer [23]. The molecular structures of these three energetic compounds are shown in Fig. 1. The addition of BTTN may practically be considered to

stoichiometrically balance the fuel-rich RDX/GAP propellant [24]. BTTN, a liquid under room conditions, has a chemical structure and composition very similar to nitrate esters, most notably nitroglycerin (NG). It is an energetic compound that undergoes self-sustained deflagration and the adiabatic flame temperature, calculated using the CEC code [25], was about 3070 K at 1 atm. Such a high flame temperature is attributed to the stoichiometrically balanced character of BTTN. The viscosity is 59 centipoise at 298 K and heat of combustion is 2168 cal/g [26]. Pudupakkam [27] recently developed a one-dimensional model of BTTN combustion, which accounts for the physicochemical processes in the condensed and gas phases, as well as the thermodynamic phase change at the interface. The gas phase kinetics involves 75 species and 462 reactions. The calculated surface temperature was in the range of 500–600 K over the pressure between 1 and 100 atm, much lower than its counterpart of GAP [18]. The calculated temperature profile for pure BTTN reveals the existence of a dark-zone temperature plateau [27], which has also been observed in experimental studies [28].

The present work attempts to establish a comprehensive analysis for investigating the key mechanisms dictating the burning behavior and combustion-wave structure of RDX/GAP/BTTN pseudo-propellant over a broad range of pressures and preconditioned temperatures. The prefix “pseudo-” is retained to emphasize that RDX, GAP, and BTTN are mixed physically and no curing agent is used, as opposed to operational propellants. The formulation is based on the conservation equations of mass, energy, and species concentration for both the condensed and the gas phases, and takes into account finite-rate chemical kinetics and variable thermophysical properties. The results discussed here will provide a thorough exposition of the combustion mechanisms of this propellant.

2. Theoretical formulation

Fig. 2 shows snapshots of RDX/GAP/BTTN propellant burning in nitrogen at 0.92 atm [46]. The sample diameter is 10 mm. The carbonaceous layer on the propellant surface sloughs off periodically. The propellant sample burns with a rounded edge and a molten surface. The luminous flame standoff distance from the surface is around 3 mm at the center, and decreases to about 1 mm near the edge. Microthermocouples and optical diagnostics, such as saturated planar laser-induced fluorescence (PLIF), spontaneous Raman spectroscopy, and UV/visible absorption spectroscopy, were used to obtain the temperature profiles and species concentrations along the centerline [1,23].

The entire combustion-wave structure of RDX/GAP/BTTN pseudo-propellant can be segmented into three regions: solid phase, near-surface two phase, and gas phase, as shown schematically in Fig. 3. In the solid-phase region, RDX powder, GAP, and BTTN are physically mixed. RDX melts at 478 K with negligible chemical reactions taking place, due to the low temperature and short residence time. The decomposition temperature for pure BTTN is 523–773 K, according to Roos and Brill [31]. Thermal decomposition and phase change of RDX and BTTN occur to form a foam layer. The propellant surface ($x = 0$) is defined herein as the interface between the foam layer and the gas-phase region, at which rapid gasification of RDX takes place. Since the surface temperature of RDX/GAP/BTTN pseudo-propellant (~ 600 K) is lower than the gasification temperature of pure GAP (~ 1050 K), GAP leaves the surface as aerosol surrounded with the RDX and BTTN vapor and their decomposed gaseous products. The gas-phase region, where GAP particles remain as a condensed species and continue to decompose, requires a two-phase treatment.

A quasi-one-dimensional model is formulated as a first approximation to the problem with the coordinate system fixed at the propellant surface ($x = 0$).

3. Solid-phase region

Chemical reactions of RDX, GAP, and BTTN are ignored in the solid-phase region because of the low-temperature condition. Thus, only the heat conduction governed by the following equation is considered:

$$\rho_c c_c \frac{\partial T_c}{\partial t} + \rho_c u_c c_c \frac{\partial T_c}{\partial x} = \frac{\partial}{\partial x} \left(\lambda_c \frac{\partial T_c}{\partial x} \right). \quad (1)$$

The thermodynamic and transport properties used in the present work are given in Table 1. The thermal conductivities and specific heat capacities of solid RDX and liquid GAP were obtained as a function of temperature by Hanson-Parr and Parr [29], and those for BTTN from Pudupakkam [27]. Due to the lack of reliable data in the literature, the properties of solid GAP were assumed to be the same as those of their liquid counterparts. The heat of formation and density of BTTN were taken from Cruise [48]. The properties of the mixture are mass-averaged as follows:

$$\rho_c c_c = Y_{\text{RDX}} \rho_{\text{RDX}} c_{\text{RDX}} + Y_{\text{GAP}} \rho_{\text{GAP}} c_{\text{GAP}} + Y_{\text{BTTN}} \rho_{\text{BTTN}} c_{\text{BTTN}}, \quad (2)$$

$$\lambda_c = Y_{\text{RDX}} \lambda_{\text{RDX}} + Y_{\text{GAP}} \lambda_{\text{GAP}} + Y_{\text{BTTN}} \lambda_{\text{BTTN}}. \quad (3)$$

A closed-form solution to Eq. (1) at steady state is available, subject to appropriate boundary conditions and propellant burning rate.

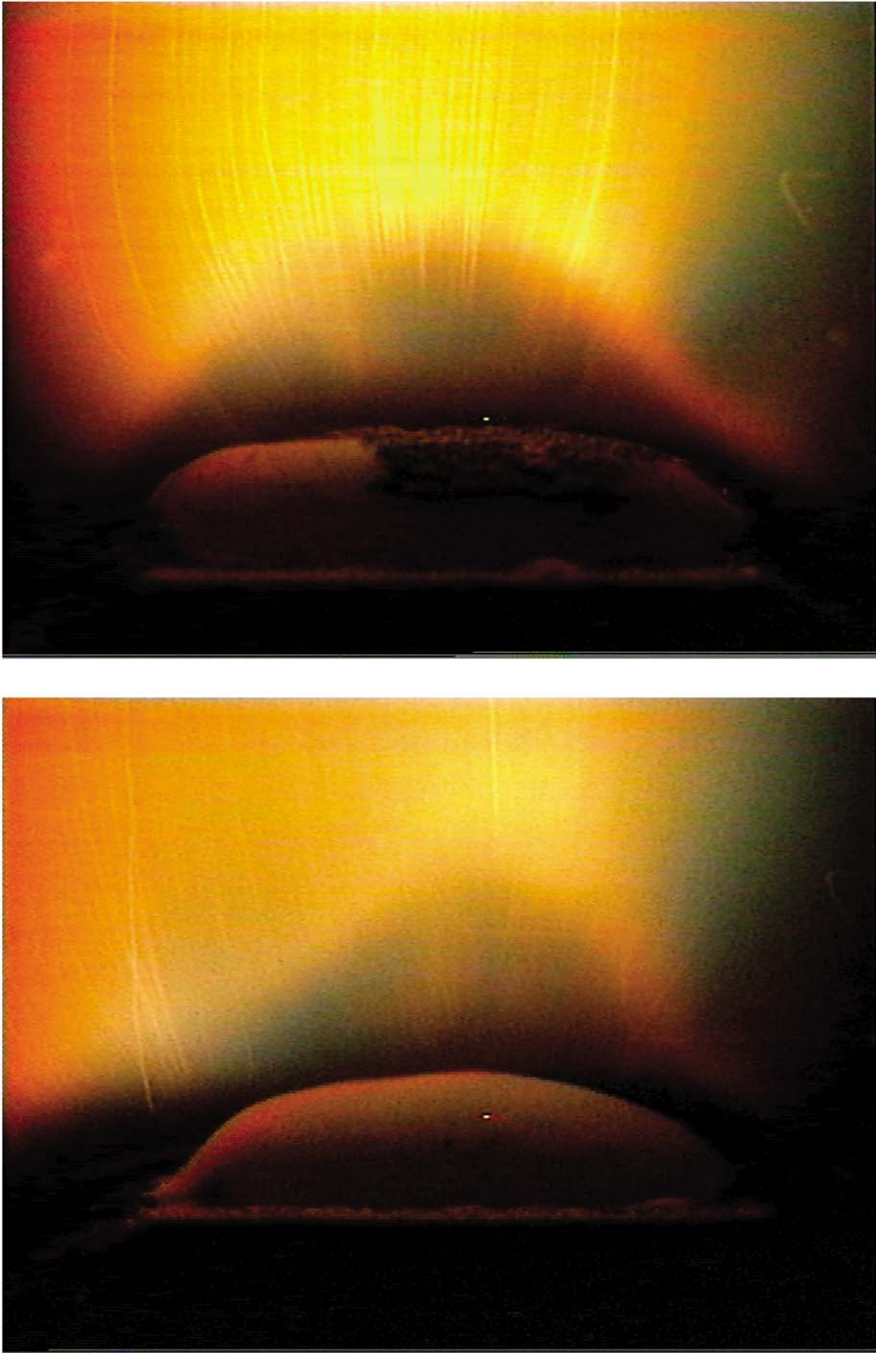


Fig. 2. Photo images of self-sustained RDX/GAP/BTN (mass ratio 71/9/20) propellant combustion in nitrogen at 0.92 atm, showing intermittent carbonaceous residue on propellant surface (photo courtesy of Parr and Hanson-Parr [46]).

4. Subsurface multiphase region (foam layer)

A two-phase fluid dynamics model based on a spatial averaging technique [4] is employed to treat the process in the foam layer. The analysis accom-

modates thermal decomposition of RDX, GAP, and BTTN, as well as subsequent reactions. The formation of gas bubbles due to evaporation is also considered for completeness. By neglecting mass diffusion in the subsurface region, the conservation equations

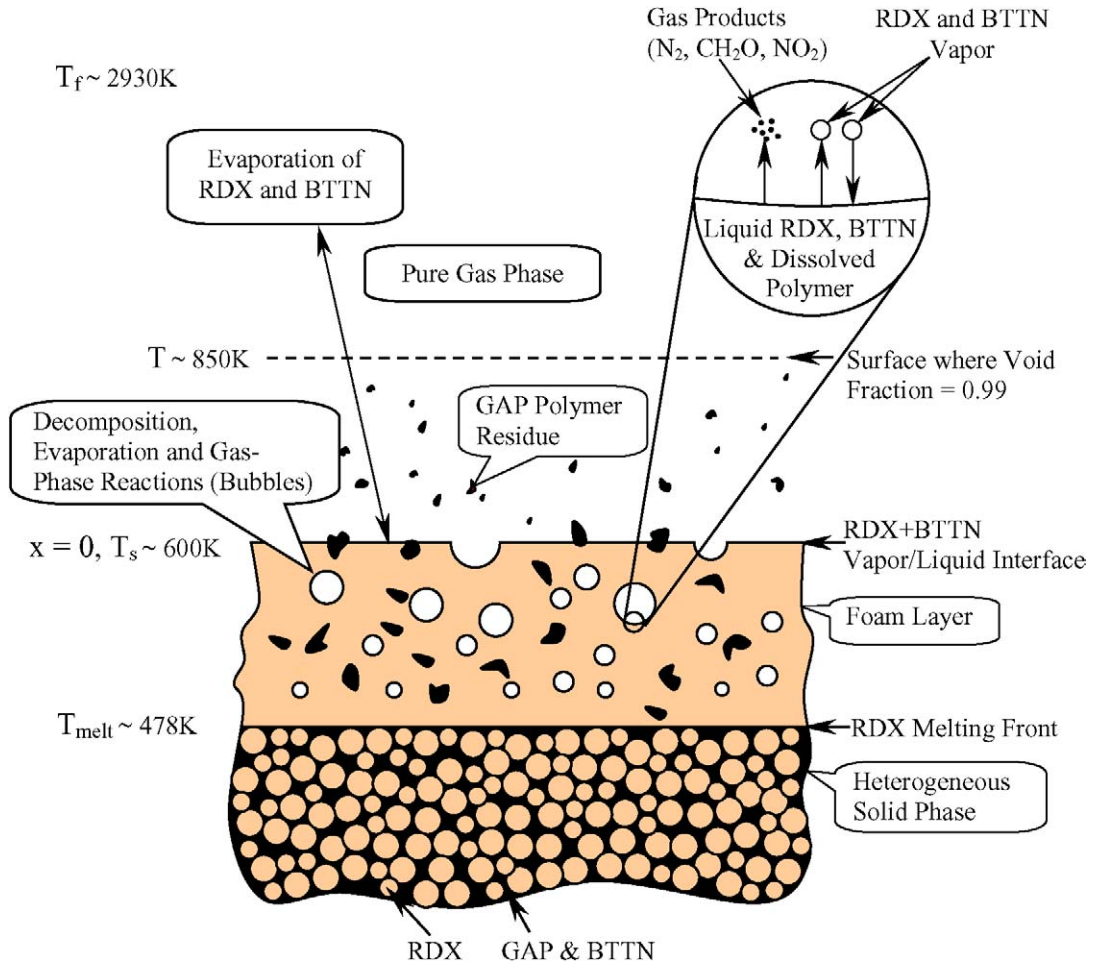


Fig. 3. Combustion-wave structure of RDX/GAP/BTTN propellant at 1 atm.

Table 1
Thermodynamic and transport properties of RDX, GAP, and BTTN

Parameter	Units	Value	Ref. or comments
$c_{p,s,RDX}$	cal/g K	$4.735 \times 10^{-3} + 0.843 \times 10^{-3} \times T$	[29]
$c_{p,l,RDX}$	cal/g K	$4.735 \times 10^{-3} + 0.843 \times 10^{-3} \times T$	$c_{p,l,RDX} = c_{p,s,RDX}$
$c_{p,l,GAP}$	cal/g K	$1.503 \times 10^{-1} + 0.966 \times 10^{-3} \times T$	[29]
$c_{p,l,BTTN}$	cal/g K	0.30	[27,47]
$\lambda_{s,RDX}$	cal/K s cm	0.665×10^{-3}	[29]
$\lambda_{l,RDX}$	cal/K s cm	0.665×10^{-3}	$\lambda_{l,RDX} = \lambda_{s,RDX}$
$\lambda_{l,GAP}$	cal/K s cm	$1.050 \times 10^{-3} - 0.146 \times 10^{-5} \times T$	[29]
$\lambda_{l,BTTN}$	cal/K s cm	0.63×10^{-3}	[27,47]
$\rho_{s,RDX}$	G/cm ³	1.806	[40]
$\rho_{l,RDX}$	G/cm ³	1.806	$\rho_{s,RDX} = \rho_{l,RDX}$
$\rho_{l,GAP}$	G/cm ³	1.30	[16]
$\rho_{l,BTTN}$	G/cm ³	1.521	[29,48]
$H_{v,RDX}$	kcal/mol	26.8	[8]
$H_{v,BTTN}$	kcal/mol	21.517	[27,47]
$T_{m,RDX}$	K	478	[40]

for both the condensed and the gas phases can be written as follows:

mass

$$\frac{\partial[(1 - \phi_f)\rho_c + \phi_f\rho_g]}{\partial t} + \frac{\partial}{\partial x}[(1 - \phi_f)\rho_c u_c + \phi_f\rho_g u_g] = 0, \quad (4)$$

condensed species concentration

$$\frac{\partial[(1 - \phi_f)\rho_c Y_{c_i}]}{\partial t} + \frac{\partial}{\partial x}[(1 - \phi_f)\rho_c u_c Y_{c_i}] = \dot{w}_{c_i} \quad (i = 1, 2, \dots, N_c), \quad (5)$$

gaseous species concentration

$$\frac{\partial(\phi_f\rho_g Y_{g_i})}{\partial t} + \frac{\partial(\phi_f\rho_g u_g Y_{g_i})}{\partial x} = \dot{w}_{g_i} \quad (i = 1, 2, \dots, N_g), \quad (6)$$

energy

$$\begin{aligned} \rho_f c_f \frac{\partial T_f}{\partial t} - \frac{\partial p}{\partial t} + \rho_f u_f c_f \frac{\partial T_f}{\partial x} \\ = \frac{\partial}{\partial x} \left(\lambda_f \frac{\partial T_f}{\partial x} \right) - \sum_{j=1}^{N_g} \dot{w}_{g_j} h_{g_j} - \sum_{j=1}^{N_c} \dot{w}_{c_j} h_{c_j} \\ + \sum_{j=1}^{N_g} h_{g_j} Y_{g_j} \dot{w}_{c-g} - \sum_{j=1}^{N_c} h_{c_j} Y_{c_j} \dot{w}_{c-g}, \end{aligned} \quad (7)$$

where \dot{w}_{c-g} represents the rate of mass conversion from liquid to gas. The subscripts f , c , and g refer to the foam layer, condensed phase, and gas phase, respectively. The properties of liquid RDX are assumed to be identical to those at the solid state. The thermo-physical properties are mass-averaged as follows:

$$\rho_f c_f = (1 - \phi_f)\rho_c c_c + \phi_f\rho_g c_g, \quad (8)$$

$$\rho_f u_f c_f \equiv (1 - \phi_f)\rho_c u_c c_c + \phi_f\rho_g u_g c_g, \quad (9)$$

$$\lambda_f = \frac{[(1 - \phi_f)\rho_c u_c \lambda_c + \phi_f\rho_g u_g \lambda_g]}{[(1 - \phi_f)\rho_c u_c + \phi_f\rho_g u_g]}, \quad (10)$$

where

$$c_c = \sum_{i=1}^{N_c} c_{c_i} Y_{c_i}, \quad (11a)$$

$$c_g = \sum_{i=1}^{N_g} c_{g_i} Y_{g_i}, \quad (11b)$$

$$\lambda_c = \sum_{i=1}^{N_c} \lambda_{c_i} Y_{c_i}, \quad \text{and} \quad (11c)$$

$$\lambda_g = \sum_{i=1}^{N_g} \lambda_{g_i} Y_{g_i}. \quad (11d)$$

The mass and energy production terms in Eqs. (5)–(7) depend on the specific chemical reaction mechanisms employed and can be formulated as described below.

In the subsurface region, two global decomposition pathways are employed for RDX (R1 and R2), two for GAP (R3 and R4), and one for BTTN (R11), as listed in Table 2. Reaction (R1) is a water-catalyzed exothermic reaction to form CH₂O and NO₂, and is favored at low heating-rate conditions. Reaction (R2) is endothermic and prevails at high temperatures. Subsequent reactions among the products of (R1) and (R2) then occur to provide the thermal energy to sustain the pyrolysis in condensed-phase materials. Brill [30] indicated that the reaction between CH₂O and NO₂ (R6) is probably the most important secondary reaction in the foam layer. The rate parameters of reaction (R6) were determined with shock-tube experiments [33]. Thermodynamic phase transition consisting of evaporation and condensation of RDX (R5) and BTTN (R12) is considered to provide a complete description of the mass transfer process.

The GAP sample considered in the present study is composed of 56 monomer units and is denoted as “GAP56.” There is universal agreement that GAP decomposition is initiated by the bond cleavage of the azide group releasing N₂ and GAP56* [11–17,32, 35], as given by reaction (R3) in Table 2. This bond-breaking process proceeds rapidly over a temperature range from 533 to 563 K, and has activation energy of about 41 kcal/mol [16]. We assume a first-order reaction with the preexponential factor and activation energy deduced by Sysak et al. [34]. The subsequent decomposition of GAP, which is rapid and highly exothermic, releases NH₃ along with HCN, CO, CH₂O, CH₂CO, CH₄, C₂H₄, H₂O, and GAP oligomers [16]. A species balance of the data acquired from a laser-assisted combustion study of GAP polyol by Tang et al. [17] leads to a global reaction model (R4) for the decomposition of GAP56*. The subsequent reactions ((R7), (R8), (R9), and (R10)) of the gaseous decomposition products from GAP are listed in Table 2. To allow the reduction of aldehydes (CH₃CHO and C₂H₃CHO) and imines (CH₃CHNH and CH₂CHCHNH), bimolecular decomposition reactions are formulated, with the activation energies being more-or-less equal to the difference in enthalpy between products and reactants. The preexponential factors are assigned values that are typical for such a process, as given in Table 2.

Addition of the oxygen-rich plasticizer BTTN makes the overall propellant more stoichiometrically balanced and thus helps reduce the formation of carbonaceous residue on the propellant surface [24]. The initial decomposition step in BTTN combustion is probably the scission of the O–NO₂ bond [28,31,32]. CH₂O and NO₂ are the main products

Table 2
Subsurface chemical reactions and rate parameters

No.	Reaction	$A^{a,c}$	$E^{b,c}$
R1	$\text{RDX}_{(l)} \rightarrow 3\text{CH}_2\text{O} + 3\text{N}_2\text{O}$	6×10^{13}	36,000
R2	$\text{RDX}_{(l)} \rightarrow 3\text{HCN} + 1.5(\text{NO}_2 + \text{NO} + \text{H}_2\text{O})$	2.5×10^{16}	44,100
R3	$\text{GAP56}_{(l)} \rightarrow \text{GAP56}_{(l)}^* + 56\text{N}_2$	5×10^{15}	41,500
R4	$\text{GAP56}_{(l)}^* \rightarrow 25.6\text{HCN} + 15.8\text{CO} + 14.4\text{NH}_3 + 17.8\text{CH}_2\text{O}$ $+ 16\text{CH}_3\text{CHO} + \text{H}_2\text{O} + 6.4\text{C}_2\text{H}_3\text{CHO} + 1.5\text{C}_2\text{H}_4$ $+ 8\text{CH}_3\text{CHNH} + 8\text{CH}_2\text{CHCHNH} + 14.6\text{C}_{(s)}$	1.28×10^{19}	53,000
R5	$\text{RDX}_{(l)} \rightleftharpoons \text{RDX}_{(g)}$	Gas kinetic theory	–
R6	$\text{CH}_2\text{O} + \text{NO}_2 \rightarrow \text{CO} + \text{NO} + \text{H}_2\text{O}$	$802 \times T^{2.77}$	13,730
R7	$\text{CH}_3\text{CHO} + \text{M} = \text{CH}_3 + \text{HCO} + \text{M}$	7×10^{15}	81,770
R8	$\text{C}_2\text{H}_3\text{CHO} + \text{M} = \text{C}_2\text{H}_3 + \text{HCO} + \text{M}$	10^{16}	97,600
R9	$\text{CH}_3\text{CHNH} + \text{M} = \text{CH}_3 + \text{H}_2\text{CN} + \text{M}$	10^{16}	63,700
R10	$\text{CH}_2\text{CHCHNH} + \text{M} = \text{C}_2\text{H}_3 + \text{H}_2\text{CN} + \text{M}$	10^{16}	66,900
R11	$\text{BTTN}_{(l)} \rightarrow 2.2\text{NO} + 2.2\text{CO} + 1.1\text{H}_2 + 0.6\text{O}_2 + 0.6\text{CO}_2$ $+ 0.4\text{CH}_4 + 1.0\text{H}_2\text{O} + 0.1\text{C}_2\text{H}_2 + 0.2\text{HCN} + 0.1\text{N}_2$ $+ 0.4\text{CH}_2\text{O} + 0.4\text{NO}_2$	0.1×10^{17}	40,000
R12	$\text{BTTN}_{(l)} \rightleftharpoons \text{BTTN}_{(g)}$	$1.2352 \times 10^{15}/p$	21,517

^a A , preexponential factor.

^b E , activation energy.

^c Units are in mol, cm, s, K, and cal.

at low pressure, along with some CO and NO. The concentrations of NO₂ and NO were reported [31] to increase with the increasing number of –ONO₂, while that of CH₂O increases with the number of –CH₂O– groups in the parent nitrate ester. Owing to the secondary reactions involving CH₂O and NO₂, which produce NO, CO, and H₂O [31], the concentrations of CH₂O and NO₂ were observed to decrease with increasing pyrolysis temperature and pressure. This is attributed to the fact that at higher temperatures and pressures, the reactions by which CH₂O and NO₂ are formed from nitrate esters are overshadowed by reactions leading to NO and CO [31]. The condensed-phase global decomposition reaction for BTTN used in the model, given by reaction (R11) in Table 2, is based on the experimental data of Parr and Hanson-Parr [28] and Roos and Brill [31]. NO and CO are the major products in this reaction. Since H₂O was measured as a major product in Ref. [28] and H₂ and O₂ as major products in Ref. [31], the model uses a mixture of these species [27,47]. The activation energy of 40 kcal/mol is based on the nitrate ester literature [36,37]. The evaporation of BTTN_(l) is modeled with reaction (R12) in Table 2 [27,47].

Based on the chemical mechanisms given by (R1)–(R12), the species production terms for the subsurface reactions in Eqs. (5) and (6) are listed in Table 3. The forward and backward reactions in (R5) and (R12) denote the evaporation and condensation processes of RDX and BTTN between the liquid and the vapor phases, respectively. The production terms

in Table 3 are given by

$$\dot{w}_{R1} = (1 - \phi_f)\rho_c Y_{c,1} k_1, \quad (12)$$

$$\dot{w}_{R2} = (1 - \phi_f)\rho_c Y_{c,1} k_2, \quad (13)$$

$$\dot{w}_{R3} = (1 - \phi_f)\rho_c Y_{c,3} k_3, \quad (14)$$

$$\dot{w}_{R4} = (1 - \phi_f)\rho_c Y_{c,4} k_4, \quad (15)$$

$$\begin{aligned} \dot{w}_{R5} &= A_s(k_{5f} - k_{5b}) \\ &= A_s s \bar{v}_n C_{\text{RDX}} \left(\frac{p_{v,\text{eq}}}{p} - X_{g,5} \right), \end{aligned} \quad (16)$$

$$\begin{aligned} \dot{w}_{R12} &= A_s(k_{12f} - k_{12b}) \\ &= A_s s \bar{v}_n C_{\text{BTTN}} \left(\frac{p_{v,\text{eq}}}{p} - X_{g,12} \right), \end{aligned} \quad (17)$$

where

$$s = 1 \quad \text{and} \quad p_{v,\text{eq}} = p_0 \exp\left(-\frac{H_v}{R_u T}\right), \quad (18)$$

$$\dot{w}_{R6} = \phi_f k_6 \left(\frac{\rho_g Y_{g,6}}{W_6} \right) \left(\frac{\rho_g Y_{g,9}}{W_9} \right), \quad (19)$$

$$\dot{w}_{R11} = (1 - \phi_f)\rho_c Y_{c,11} k_{11}. \quad (20)$$

5. Gas-phase region

The species in the gas phase include vapor RDX and BTTN, products of RDX, GAP, and BTTN decomposition and their subsequent reactions, and unreacted GAP aerosol. Since condensed and gaseous species both exist in this region, a two-phase treatment similar to that described in the preceding section

Table 3
Description of species formation in foam layer

I	Species	\dot{w}_{c_i} or \dot{w}_{g_i}
1	RDX _(l)	$-(\dot{w}_{R1} + \dot{w}_{R2} + \dot{w}_{R5})$
2	GAP56 _(l)	$-\dot{w}_{R3}$
3	GAP56* _(l)	$\dot{w}_{R3}W_3/W_2 - \dot{w}_{R4}$
4	C _(s)	$14.6\dot{w}_{R4}W_4/W_3$
5	RDX _(g)	\dot{w}_{R5}
6	CH ₂ O	$W_6(3\dot{w}_{R1}/W_1 + 17.8\dot{w}_{R4}/W_3 - \dot{w}_{R6} + 0.4\dot{w}_{R11}/W_{26})$
7	N ₂ O	$W_7(3\dot{w}_{R1}/W_1)$
8	HCN	$W_8(3\dot{w}_{R2}/W_1 + 25.6\dot{w}_{R4}/W_3 + 0.2\dot{w}_{R11}/W_{26})$
9	NO ₂	$W_9(1.5\dot{w}_{R2}/W_1 - \dot{w}_{R6} + 0.4\dot{w}_{R11}/W_{26})$
10	NO	$W_{10}(1.5\dot{w}_{R2}/W_1 + \dot{w}_{R6} + 2.2\dot{w}_{R11}/W_{26})$
11	H ₂ O	$W_{11}(1.5\dot{w}_{R2}/W_1 + \dot{w}_{R4}/W_3 + \dot{w}_{R6} + 1.0\dot{w}_{R11}/W_{26})$
12	N ₂	$W_{12}(56\dot{w}_{R3}/W_2 + 0.1\dot{w}_{R11}/W_{26})$
13	CO	$W_{13}(15.8\dot{w}_{R4}/W_3 + \dot{w}_{R6} + 2.2\dot{w}_{R11}/W_{26})$
14	NH ₃	$W_{14}(14.4\dot{w}_{R4}/W_3)$
15	C ₂ H ₄	$W_{15}(1.5\dot{w}_{R4}/W_3)$
16	CH ₃ CHO	$W_{16}(16\dot{w}_{R4}/W_3) - \dot{w}_{R7}$
17	C ₂ H ₃ CHO	$W_{17}(6.4\dot{w}_{R4}/W_3) - \dot{w}_{R8}$
18	CH ₃ CHNH	$W_{18}(8\dot{w}_{R4}/W_3) - \dot{w}_{R9}$
19	CH ₂ CHCHNH	$W_{19}(8\dot{w}_{R4}/W_3) - \dot{w}_{R10}$
20	BTTN _(g)	\dot{w}_{R12}
21	H ₂	$W_{21}(1.1\dot{w}_{R11}/W_{26})$
22	O ₂	$W_{22}(0.6\dot{w}_{R11}/W_{26})$
23	CO ₂	$W_{23}(0.6\dot{w}_{R11}/W_{26})$
24	CH ₄	$W_{24}(0.4\dot{w}_{R11}/W_{26})$
25	C ₂ H ₂	$W_{25}(0.1\dot{w}_{R11}/W_{26})$
26	BTTN _(l)	$-\dot{w}_{R11} - \dot{w}_{R12}$

is employed to formulate the problem. The flow cross-section area, however, varies due to the flame expansion effects. Ignoring body force, viscous dissipation, and radiation emission/absorption effects, the isobaric conservation equations for both the condensed and the gas phases can be written as follows:

mass

$$\frac{\partial[(1 - \phi_g)A\rho_c + \phi_g A\rho_g]}{\partial t} + \frac{\partial}{\partial x}[(1 - \phi_g)A\rho_c u_c + \phi_g A\rho_g u_g] = 0, \quad (21)$$

condensed species concentration

$$\frac{\partial[(1 - \phi_g)A\rho_c Y_{c_i}]}{\partial t} + \frac{\partial}{\partial x}[(1 - \phi_g)A\rho_c u_c Y_{c_i}] = A\dot{w}_{c_i} \quad (i = 1, 2, \dots, N_c), \quad (22)$$

gaseous species concentration

$$\phi_g A\rho_g \frac{\partial Y_{g_i}}{\partial t} + \phi_g A\rho_g u_g \frac{\partial Y_{g_i}}{\partial x} + \frac{\partial(\phi_g A\rho_g V_{g_i} Y_{g_i})}{\partial x} = A\dot{w}_{g_i} - Y_{g_i} A\dot{w}_{c-g} \quad (i = 1, 2, \dots, N_g), \quad (23)$$

energy

$$\rho c_p A \frac{\partial T_g}{\partial t} - \frac{\partial(pA)}{\partial t} + \rho u c_p A \frac{\partial T_g}{\partial x}$$

$$= \frac{\partial}{\partial x} \left(\lambda A \frac{\partial T_g}{\partial x} \right) - \phi_g A \sum_{j=1}^{N_g} \rho_g Y_{g_j} V_{g_j} c_{p_{g_j}} \frac{\partial T_g}{\partial x} - A \sum_{j=1}^{N_g} \dot{w}_{g_j} h_{g_j} - A \sum_{j=1}^{N_c} \dot{w}_{c_j} h_{c_j} + A \sum_{j=1}^{N_g} h_{g_j} Y_{g_j} \dot{w}_{c-g} - A \sum_{j=1}^{N_c} h_{c_j} Y_{c_j} \dot{w}_{c-g}, \quad (24)$$

where the subscripts *c* and *g* denote the condensed and gas phases, respectively. The thermophysical and flow properties are mass-averaged as follows:

$$\rho c_p = (1 - \phi_g)\rho_c c_{c_p} + \phi_g \rho_g c_{g_p}, \quad (25)$$

$$\rho u c_p = (1 - \phi_g)\rho_c u_c c_{c_p} + \phi_g \rho_g u_g c_{g_p}, \quad (26)$$

$$\lambda_g = \left[(1 - \phi_g)\rho_c u_c \lambda_c + \phi_g \rho_g u_g \lambda_g \right] / \left[(1 - \phi_g)\rho_c u_c + \phi_g \rho_g u_g \right]. \quad (27)$$

The enthalpy of gaseous or condensed species *i* in Eq. (24) is defined as

$$h_i = \int_{T_{ref}}^T c_{p_i} dT + h_{f_i}^\circ. \quad (28)$$

The mass diffusion velocity V_i consists of contributions from both concentration and temperature gradients,

$$V_i = -D_i \frac{1}{X_i} \frac{\partial X_i}{\partial x} + D_i \frac{DT_i}{X_i T} \frac{\partial T}{\partial x}. \quad (29)$$

Finally, the equation of state for a multicomponent system is used to close the formulation

$$p = \rho_g R_u T_g \sum_{i=1}^{N_g} \frac{Y_{g_i}}{W_{g_i}}. \quad (30)$$

The chemical reactions can be written in the following general form:



where v'_{ij} and v''_{ij} are the stoichiometric coefficients for the i th species appearing as a reactant in the j th forward and backward reactions, respectively, and M_i is the chemical symbol for the i th species. The reaction rate constant k_j (either k_{fj} or k_{bj}) is given by the Arrhenius expression

$$k_j = A_j T^{B_j} \exp(-E_j/R_u T). \quad (32)$$

The rate of change of molar concentration of species i by reaction j is

$$\dot{C}_{ij} = (v'_{ij} - v''_{ij}) \times \left(k_{fj} \prod_{i=1}^{N_g} C_i^{v'_{ij}} - k_{bj} \prod_{i=1}^{N_g} C_i^{v''_{ij}} \right). \quad (33)$$

The total mass production rate of gaseous species i in Eq. (23) is then obtained by summing up the changes due to all gas-phase and condensed-phase reactions,

$$\dot{w}_{g_i} = \phi_g W_{g_i} \sum_{j=1}^{N_R} \dot{C}_{ij} + \dot{w}_{c-g, g_i}, \quad (34)$$

where \dot{w}_{c-g, g_i} represents the mass conversion rate from liquid to gas of gaseous species i .

The gas-phase chemical kinetics scheme is composed of five submodels:

- (1) the RDX combustion mechanism [7],
- (2) the additional reactions, recently proposed by Chakraborty and Lin [38], involving the consumption of H_2CNNO_2 , H_2CNNO , H_2CNO , H_2CNOH , and H_2CN ,
- (3) the initial decomposition reactions of GAP including, among others, aldehydes and imines,
- (4) the initial decomposition reactions of BTTN [28, 31,47], and

- (5) the hydrocarbon combustion mechanism [39] containing 49 species and 279 reactions.

The species mass production rates generated by condensed-phase reactions in Eqs. (22) and (23) are described by reactions (R3) and (R4) of condensed GAP and its intermediate products. Overall, the gas-phase kinetics involves 72 species and 429 reactions to allow for detailed investigation of the heat-release mechanisms.

6. Boundary conditions

The processes in the gas-phase region and subsurface foam layer must be matched at the propellant surface ($x = 0$) to provide the boundary conditions for each region. This procedure requires balances of mass and energy, and eventually determines propellant surface conditions and burning rate. By neglecting mass diffusion in the condensed phase, the conservation laws at the propellant surface can be written as follows:

mass

$$[(1 - \phi_f) \rho_c u_c + \phi_f \rho_g u_g]_{0^-} = [(1 - \phi_g) \rho_c u_c + \phi_g \rho_g u_g]_{0^+}, \quad (35)$$

species

$$[(1 - \phi_f) \rho_c u_c Y_{c_i} + \phi_f \rho_g u_g Y_{g_i}]_{0^-} = [(1 - \phi_g) \rho_c u_c Y_{c_i} + \phi_g \rho_g (u_g + V_{g_i}) Y_{g_i}]_{0^+}, \quad (36)$$

energy

$$\left[\lambda_f \frac{dT_f}{dx} + (1 - \phi_f) \rho_c u_c Y_{RDX_c} h_{RDX_{l \rightarrow g}} + (1 - \phi_f) \rho_c u_c Y_{BTTN_c} h_{BTTN_{l \rightarrow g}} \right]_{0^-} = \left[\lambda_g \frac{dT_g}{dx} \right]_{0^+}. \quad (37)$$

The temperature is identical on both sides of the interface, but the void fraction and species mass fractions are different.

Since the propellant surface is defined as the interface where rapid phase transition occurs, the evaporation law of RDX and BTTN is assumed to prevail at the interface [4], giving

$$[(1 - \phi_f) \rho_c u_c Y_{RDX_c}]_{0^-} = \left[s \bar{v}_n C_{RDX_g} \left(\frac{p_{v,eq}}{p} - X_{RDX_g} \right) \right]_{0^+}, \quad (38)$$

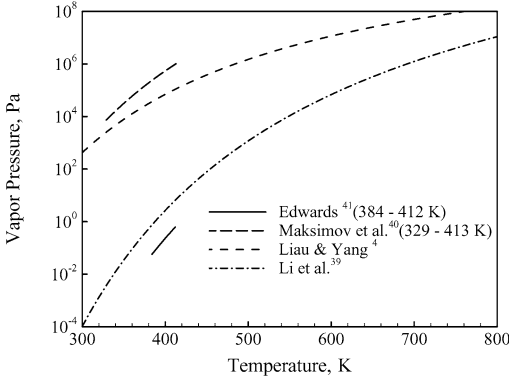


Fig. 4. Vapor pressure of pure RDX.

$$\begin{aligned}
 & [(1 - \phi_f)\rho_c u_c Y_{\text{BTTN}_c}]_{0-} \\
 &= \left[s \bar{v}_n C_{\text{BTTN}_g} \left(\frac{p_{v,\text{eq}}}{p} - X_{\text{BTTN}_g} \right) \right]_{0+}. \quad (39)
 \end{aligned}$$

Most of the existing data regarding the RDX vapor pressure, as shown in Fig. 4, is based on the sublimation of RDX [41,42]. The correlation proposed by Li et al. [40] was employed in our previous work on RDX combustion. The BTTN vapor pressure is 7466 Pa at 397 K [26] and the temperature dependence is taken from Puduppakkam and co-workers [27,47].

It has been shown that $\rho_c u_c = \rho_g u_g$ is a good assumption for modeling the two-phase process in nitramine propellant combustion [4]. Equation (35) thus becomes trivial and Eq. (36) can be written as follows:

$$\begin{aligned}
 & [(1 - \phi_f)Y_{c_i} + \phi_f Y_{g_i}]_{0-} \\
 &= \left[(1 - \phi_g)Y_{c_i} + \phi_g \left(1 + \frac{V_{g_i}}{u_g} \right) Y_{g_i} \right]_{0+}. \quad (40)
 \end{aligned}$$

A summation of the above equations for all the condensed species, $\text{BTTN}_{(l)}$, $\text{GAP}_{(l)}$, $\text{GAP}_{(l)}^*$, and $\text{C}_{(s)}$, gives

$$[(1 - \phi_f)(1 - Y_{\text{RDX}_c})]_{0-} = [(1 - \phi_g)]_{0+}. \quad (41)$$

Equations (37)–(41) are sufficient to solve the set of unknowns (u , T , Y_i , ϕ) at the propellant surface and provide the interfacial boundary conditions for the foam layer and gas phase.

The boundary conditions at the melting front between the solid phase and the foam layer are

$$T_c = T_f = T_{\text{melt}} \quad \text{and} \quad \phi_f = 0 \quad \text{at} \quad x = x_{\text{melt}}, \quad (42)$$

$$\begin{aligned}
 & \left[\lambda_c \frac{dT_c}{dx} + \rho_c u_c Y_{\text{RDX}} h_{\text{RDX}_{s \rightarrow l}} \right]_{x_{\text{melt}}^-} \\
 &= \left[\lambda_f \frac{dT_f}{dx} \right]_{x_{\text{melt}}^+}. \quad (43)
 \end{aligned}$$

The far-field conditions for the gas phase require the gradients of flow properties to be zero

$$\frac{\partial \rho}{\partial x} = \frac{\partial u}{\partial x} = \frac{\partial Y_i}{\partial x} = \frac{\partial T}{\partial x} = 0 \quad \text{at} \quad x = \infty. \quad (44)$$

The condition at the cold boundary for the condensed phase ($x = -\infty$) is

$$T_c = T_i \quad \text{as} \quad x \rightarrow -\infty, \quad (45)$$

where T_i is the preconditioned temperature of the propellant. The initial mass fractions of RDX, BTTN, and GAP are provided as input parameters.

7. Numerical method

The theoretical formulation established in the current work requires a robust computational scheme to handle the numerical stiffness caused by chemical reactions and transport processes. All the conservation equations and associated boundary conditions are coupled and solved by a double-iteration procedure which treats the propellant surface temperature T_s and burning rate r_b as eigenvalues. The procedure continues with T_s adjusted within the inner loop while r_b is corrected in the outer iteration. The conservation equations for the subsurface region are solved first, and the resulting species concentrations at the surface are used as the boundary conditions for the gas-phase region through the interfacial matching conditions. The next step involves integration of the gas-phase conservation equations to provide the temperature and species-concentration profiles. The non-equilibrium evaporation equations ((38) and (39)) are then employed to check the convergence of T_s . If this is not successful, another inner iteration is performed using an updated value of T_s . The outer iteration follows the same procedure as the inner loop, except that r_b is used as the eigenvalue to check the interfacial energy continuity, Eq. (37). Since only the burning rate and surface temperature, and not the interfacial species composition, are involved in the iterative procedure, the present algorithm performs quite well and significantly reduces the computational burden.

The conservation equations ((4)–(7)) for the subsurface region are fully coupled. They are, however, solved by an uncoupled-iteration method. A temperature profile is first estimated by solving an inert energy equation, and then the conservation equations of mass and species concentrations are integrated using a fourth-order Runge–Kutta method. Equation (7) is subsequently solved with the newly obtained void fraction and species concentrations to obtain another temperature profile. Since the equations are solved separately, iteration is required to ensure a converged

solution that satisfies all the conservation laws and boundary conditions.

The governing equations ((21)–(24)) for the gas phase are solved iteratively by a method similar to the subsurface-region solver. Equation (22) is first solved using a fourth-order Runge–Kutta method to get the void fraction and mass fractions of condensed species. Equations (21)–(24) are then solved using the CHEMKIN-PREMIX [43] package with some modifications since the governing equations have been changed to account for a two-phase system.

8. Discussion of results

The combustion characteristics of RDX monopropellant are first studied as a limiting case to validate the model. Good agreement of the burning rate with the experimental measurements by Zenin [44] and Atwood et al. [45] is obtained over a pressure range of 1–100 atm. The calculated pressure exponent n for pure RDX in the burning-rate law,

$$r_b = ap^n, \tag{46}$$

is 0.862, with the units of pressure in atm. The preexponential factor a is 0.038 cm/s for $T_i = 293$ K.

After validation, the analysis is applied to investigate the combustion of RDX/GAP/BTTN (mass ratio 71/9/20) pseudo-propellant over a broad range of pressures and preconditioned temperatures. Fig. 5 shows the pressure dependence of the burning rate with an initial temperature of 293 K. The experimental data obtained by Parr and Hanson-Parr [46] for $T_i = 298$ and 373 K are also included for comparison. The calculated pressure exponent n and preexponential factor a are 0.813 and 0.0318 cm/s, respectively, matching closely the measured values of 0.79 and 0.0291 cm/s at $T_i = 298$ K. Fig. 6 shows a comparison of the calculated burning rates of pure RDX [4], GAP [18], BTTN [27], RDX/GAP (mass ratio 80/20) [19], and RDX/GAP/BTTN (mass ratio 71/9/20) propellants. The preconditioned propellant temperature is 293 K. It is worth noting that the measured burning rate for pure BTTN [26] shows an abrupt increase around 30 atm above which unstable combustion occurs due to hydrodynamic instability, as explained on the basis of the Levich criterion [27, 49]. The RDX/GAP/BTTN burning rate is lower than its counterparts for pure RDX, BTTN, and GAP, but higher than that of the RDX/GAP pseudo-propellant. The low burning rate of RDX/GAP may be attributed to the rapid decomposition of GAP near the propellant surface. The resultant gaseous nitrogen tends to push the flame away from the surface and dilutes the concentration of reactive species, thereby retarding the heat feedback from the gas phase [19,20]. Similarly,

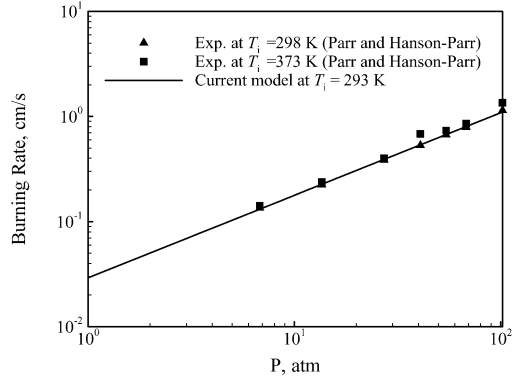


Fig. 5. Pressure dependence of burning rate of RDX/GAP/BTTN propellant (mass ratio 71/9/20); self-sustained combustion.

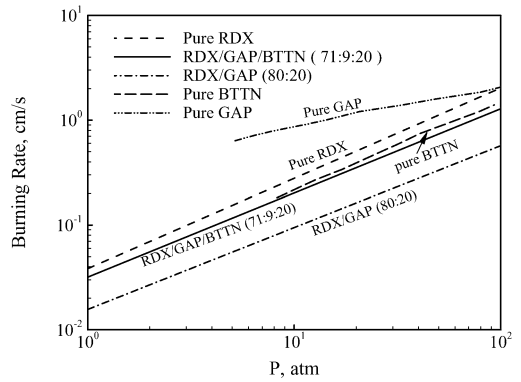


Fig. 6. Burning rates of RDX, GAP, BTTN, RDX/GAP, and RDX/GAP/BTTN propellants; self-sustained combustion at room temperature.

the inclusion of 9% GAP in the RDX/GAP/BTTN pseudo-propellant lowers the burning rate as compared to pure RDX. The addition of BTTN helps balance the fuel-rich nature of RDX/GAP (mass ratio 80/20) stoichiometrically, and thus promotes the burning.

Fig. 7 shows the calculated and measured [46] temperature sensitivity of the burning rate, defined below, at various pressures:

$$\sigma_p = \left. \frac{\partial(\ln r_b)}{\partial T_i} \right|_p. \tag{47}$$

The calculations are based on the initial temperature range of 293 ± 50 K, and indicate a decrease of σ_p from 2.5 to 1.1×10^{-3} with increasing pressure from 1 to 100 atm. At elevated pressures, the enhanced heat transfer from the gas phase to the propellant surface due to increased energy release and reduced flame standoff distance overrides the influence of preconditioned temperature in determining the energy balance at the surface, and consequently decreases the tem-

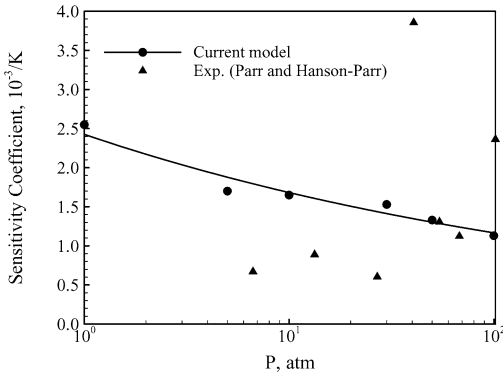


Fig. 7. Temperature sensitivity of burning rate of RDX/GAP/BTTN propellant (mass ratio 71/9/20); self-sustained combustion.

perature sensitivity of the burning rate [4,20]. The experimental data [46], however, do not show any particular trend. This may be attributed to the difficulties in measuring temperature sensitivity. The relatively low sensitivity of pure RDX, within the data scatter, also contributes to the measured behavior.

Fig. 8 compares the adiabatic flame temperatures and final species concentrations of RDX/GAP/BTTN (mass ratio 71/9/20) pseudo-propellant as predicted by the present analysis and the Chemical Equilibrium Calculations (CEC) code [25] over a pressure range of 1 to 100 atm. The preconditioned propellant temperature is 293 K. The symbols represent the present work and the solid lines the predictions by CEC. The flame temperature increases with increasing pressure. The discrepancy between the CEC and the current analysis is practically zero for 1 atm, and increases slightly to 57 K for 100 atm. The predicted flame temperature of 2933 K at 1 atm is greater than the measured value of 2850 K [23], mainly due to the heat loss to the ambient gases in the experiment. Compared with the flame temperature (i.e., 2670 K at 1 atm and 2880 K at 100 atm) of RDX/GAP (mass ratio 80/20), the higher flame temperature (i.e., 2933 K at 1 atm and 3256 K at 100 atm) of the present RDX/GAP/BTTN propellant confirms its stoichiometrically more balanced nature. The predicted N_2 mole fraction is almost identical to the CEC calculation. The present analysis, however, slightly overpredicts the CO_2 and H_2O concentrations and underpredicts the CO and H_2 concentrations in comparison with the CEC calculations. The maximum deviations in mole fractions of major species are less than 10%. A similar trend was obtained by Puduppakkam and Beckstead [47].

Fig. 9 shows the surface temperature of the RDX/GAP/BTTN (mass ratio 71/9/20) pseudo-propellant. Only one measurement of 605 K at 0.92 atm, by Parr and Hanson-Parr [23], is available. The solid and dashed lines represent the current predictions based

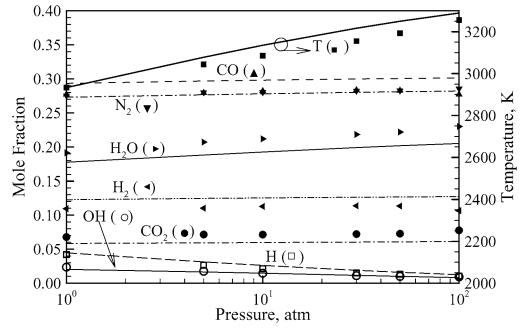


Fig. 8. Adiabatic flame temperature and final species concentrations of RDX/GAP/BTTN propellant (mass ratio 71/9/20) at $T_i = 293$ K. Symbols represent present analysis and lines represent the chemical equilibrium calculations.

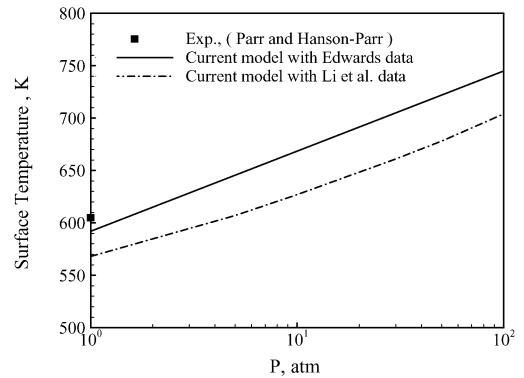


Fig. 9. Surface temperature of RDX/GAP/BTTN (mass ratio 71/9/20) propellant; self-sustained combustion burning at $T_i = 293$ K.

on the RDX vapor pressure obtained by Li et al. [40] and Edwards [42], respectively. The surface temperature depends significantly on the RDX vapor pressure, due to the prevalence of RDX evaporation in determining the propellant surface condition. In contrast, the calculated burning rate is not greatly affected by the RDX vapor pressure, since the burning rate is dictated mainly by the heat feedback from the gas phase, and not just by the thermodynamic phase change of RDX.

Fig. 10 shows the calculated temperature profile in the gas phase. The result is compared with the measured data along the centerline, at 0.92 atm, which reveals the existence of a dark-zone temperature plateau with a length of 1.5 mm and a temperature around 1200 K. Unlike the experimental observation, the present analysis yields a monotonic increase in temperature. The predicted flame standoff distance of 1 mm is slightly shorter than the measured value of 2 mm, which may possibly be due to the ambiguity inherent in defining the propellant surface during experiments. Parr and Hanson-Parr [23]

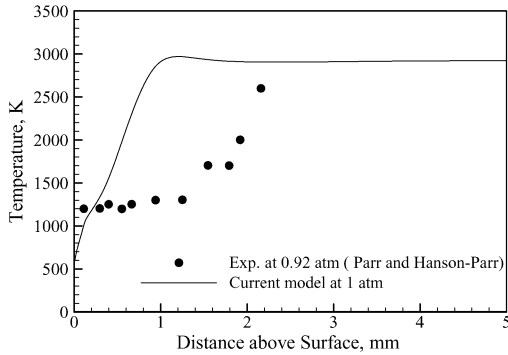


Fig. 10. Calculated and measured temperature profiles; self-sustained combustion of RDX/GAP/BTTN (mass ratio 71/9/20) at room temperature.

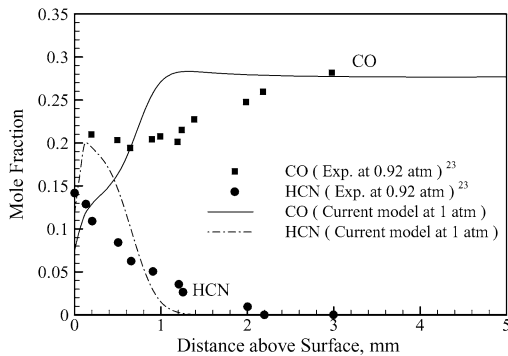


Fig. 11. Calculated and measured species profiles of CO and HCN; self-sustained combustion of RDX/GAP/BTTN (mass ratio 71/9/20) at room temperature.

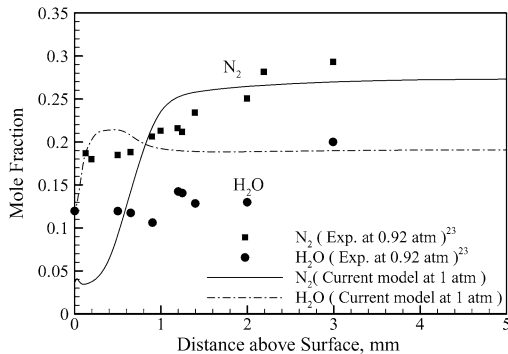


Fig. 12. Calculated and measured species profiles of N_2 and H_2O ; self-sustained combustion of RDX/GAP/BTTN (mass ratio 71/9/20) at room temperature.

reported that combustion at 0.92 atm was not entirely stable and a laser flux was used to ignite the sample, which subsequently was turned off. Figs. 11–14 show the calculated and measured species concentration profiles in the gas phase. Reasonable agreement is obtained except in the near-surface region, where

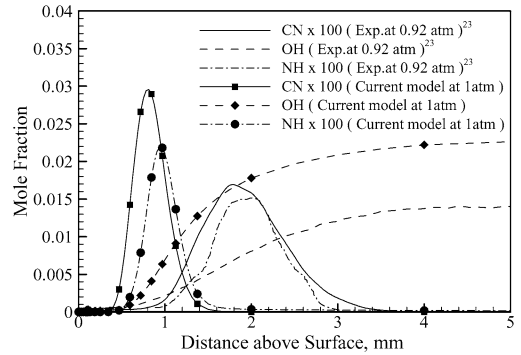


Fig. 13. Calculated and measured species profiles of OH, CN, and NH; self-sustained combustion of RDX/GAP/BTTN (mass ratio 71/9/20) at 0.92 atm and $T_i = 298$ K.

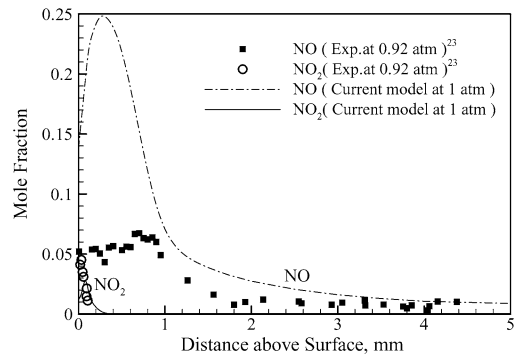


Fig. 14. Calculated and measured species profiles of NO and NO_2 ; self-sustained combustion of RDX/GAP/BTTN (mass ratio 71/9/20) at room temperature.

the model predicts lower concentrations of CO and N_2 and higher concentrations of HCN, H_2O , and NO as compared to the experimental values. Since NO, CO, and HCN are the primary species dictating the dark-zone kinetics, due to the high activation energies of their reactions, such a discrepancy in the concentration profiles is partly responsible for the lack of a temperature plateau in the calculated temperature profile. The difference in the pressure (0.92 atm in the experiments vs 1 atm in the simulation) also contributes to the disagreement in the temperature distribution. It should be noted that uncertainties exist in modeling propellant (especially BTTN) decomposition near the surface. A more detailed understanding of the chemical kinetics, in particular the initial decomposition pathways in the condensed phase and subsequent reactions among the products, is required to improve the model predictability. The situation becomes more important for low-pressure cases, in which near-surface exothermic reactions play a more dominant role in determining propellant surface conditions than the heat feedback from the gas-phase flame.

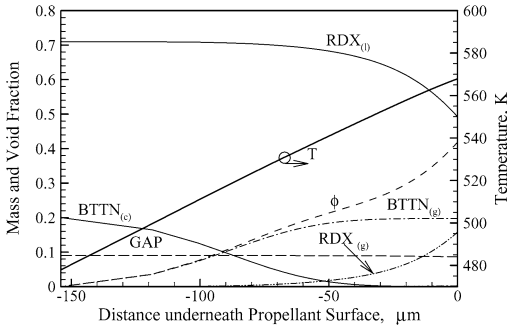


Fig. 15. Temperature and species-concentration profiles in subsurface region; self-sustained combustion of RDX/GAP/BTTN propellant (mass ratio 71/9/20) combustion at 1 atm and $T_i = 293$ K.

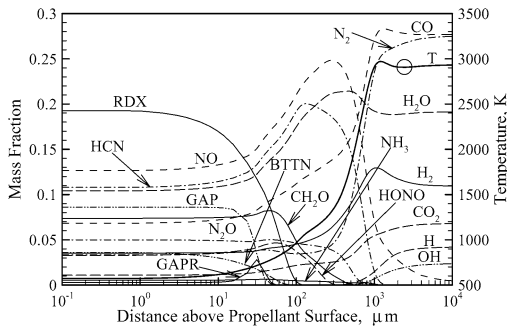


Fig. 16. Temperature and species-concentration profiles in near-surface region; self-sustained combustion of RDX/GAP/BTTN propellant (mass ratio 71/9/20) combustion at 1 atm and $T_i = 293$ K.

Fig. 15 shows the species-concentration and temperature profiles in the subsurface region. The thickness of this multiphase foam layer is about 150 μm . An appreciable amount of RDX evaporates to form gas bubbles in this region. The GAP compound, however, does not decompose in the foam layer because of the relatively low temperature of about 560 K. On the other hand, BTTN evaporates completely in this layer. The void fraction increases to about 0.4 near the surface, beyond which rapid gasification of RDX takes place.

Figs. 16 and 17 show the calculated species concentrations and temperature profiles above the propellant surface, where GAPR stands for GAP56*. The close-up view shown in Fig. 16 indicates that most of the RDX and BTTN vapor and GAP aerosol decompose within 100 μm from the surface. According to the decomposition pathways described by reactions (R1), (R2), (R4), and (R11), high concentrations of CH_2O , HCN, NO, and N_2O are present near the surface. The calculated HCN and NO concentrations attain a peak around $x = 0.2$ mm, where a narrow dark-zone temperature plateau is seen. The rapid con-

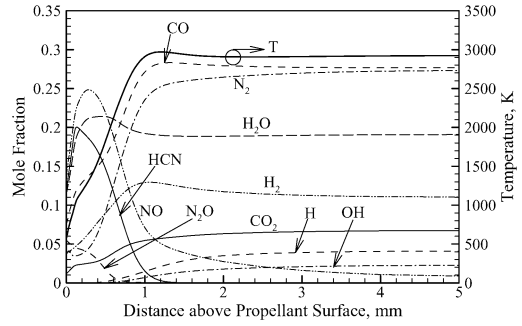
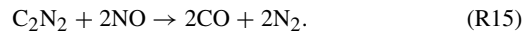
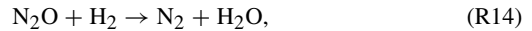
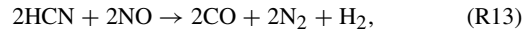


Fig. 17. Calculated species-concentration profiles in the gas-phase region; self-sustained combustion of RDX/GAP/BTTN propellant (mass ratio 71/9/20) at 1 atm and $T_i = 293$ K.

version of HCN and NO to N_2 and CO is due to the prevalence of the following reactions:



These reactions are highly exothermic and usually take place at higher temperatures, due to their large activation energies. Thus, CO and N_2 are the dominant species in the final flame zone. A significant amount of H_2O is present throughout the entire gas phase.

9. Concluding remarks

A comprehensive theoretical model and a numerical analysis have been developed to study the key physiochemical processes involved in the combustion of RDX/GAP/BTTN pseudo-propellant under steady-state conditions. The formulation is based on the conservation equations of mass, energy, and species for both the condensed and the gas phases, and takes into account finite-rate chemical kinetics, thermodynamic phase transition, and variable thermophysical properties. Results were benchmarked against measured burning rate over a pressure range of 1–100 atm, and detailed species and temperature profiles at 0.92 atm. Good agreement was obtained for the pressure sensitivity of the burning rate. The analysis, however, underpredicts CO and N_2 concentrations and overpredicts HCN, H_2O , and NO concentrations immediately above the propellant surface, mainly due to the uncertainties in modeling the initial decomposition pathways and the associated rate constants of propellant ingredients, especially for BTTN. As a consequence, the analysis does not reveal a distinct dark-zone temperature plateau which is observed experimentally. Nonetheless, the present analysis provides

a general framework for studying the detailed combustion wave structure and burning characteristics of RDX/GAP/BTTN pseudo-propellants under various operating conditions.

It is evident that more experimental data, such as the temperature sensitivity of burning rate and distributions of temperature and species concentrations, are required for further model validation over a broad range of pressures and preconditioned temperatures. The condensed-phase mechanisms and near-surface kinetics of GAP and BTTN must be explored in more detail to achieve a comprehensive understanding of RDX/GAP/BTTN pseudo-propellant combustion. The lack of reliable thermophysical properties and neglect of the flame expansion effect also limit the model accuracy.

Acknowledgments

This work was sponsored partly by the U.S. Office of Naval Research, Contract No. N00014-02-C-0292, Judah Goldwasser as Contract Monitor, and partly by the Pennsylvania State University.

References

- [1] T.P. Parr, D.M. Hanson-Parr, in: V. Yang, T.B. Brill, W.Z. Ren (Eds.), *Solid Propellant Chemistry, Combustion, and Motor Interior Ballistics*, in: *Progress in Astronautics and Aeronautics*, vol. 185, AIAA, Reston, VA, 2000, pp. 381–411.
- [2] O.P. Korobeinichev, in: V. Yang, T.B. Brill, W.Z. Ren (Eds.), *Solid Propellant Chemistry, Combustion, and Motor Interior Ballistics*, in: *Progress in Astronautics and Aeronautics*, vol. 185, AIAA, Reston, VA, 2000, pp. 335–354.
- [3] C.F. Melius, in: S. Bulusu (Ed.), *Chemistry and Physics of Energetic Materials*, Kluwer Academic, Norwell, MA, 1990, pp. 21–78.
- [4] Y.-C. Liao, V. Yang, *J. Propuls. Power* 11 (1995) 727–739.
- [5] J.E. Davidson, M.W. Beckstead, *Proc. Combust. Inst.* 26 (1996) 1989–1996.
- [6] J.E. Davidson, M.W. Beckstead, *J. Propuls. Power* 13 (1997) 375–383.
- [7] K. Prasad, R.A. Yetter, M. Smooke, *Combust. Sci. Technol.* 124 (1997) 35–82.
- [8] K. Prasad, R.A. Yetter, M. Smooke, *Combust. Flame* 115 (1998) 406–416.
- [9] M.S. Miller, W.R. Anderson, in: V. Yang, T.B. Brill, W.Z. Ren (Eds.), *Solid Propellant Chemistry, Combustion, and Motor Interior Ballistics*, in: *Progress in Astronautics and Aeronautics*, vol. 185, AIAA, Reston, VA, 2000, pp. 501–531.
- [10] Y.-C. Liao, E.S. Kim, V. Yang, *Combust. Flame* 126 (2001) 1680–1698.
- [11] M. Farber, S.P. Harris, R.D. Srivastava, *Combust. Flame* 55 (1984) 203–211.
- [12] J.E. Flanagan, D.O. Woolery, R.L. Kistner, AFAL-TR-87-107, Air Force Astronautics Laboratory, Edwards AFB, CA, 1987.
- [13] N. Kubota, T. Sonobe, *Proc. Combust. Inst.* 23 (1990) 1331–1337.
- [14] G. Lengellé, B. Fourest, J.C. Godon, C. Guin, AIAA Paper 93-2413 (1993).
- [15] A.A. Zenin, S.V. Finjakov, AIAA Paper 2000-1032 (2000).
- [16] H. Arisawa, T.B. Brill, *Combust. Flame* 112 (1998) 533–544.
- [17] C.-J. Tang, Y. Lee, T.A. Litzinger, *Combust. Flame* 117 (1999) 244–256.
- [18] K. Puduppakkam, M.W. Beckstead, *Proc. 37th JANNAF Combustion Subcommittee Meeting*, CPIA Publ. Columbia, MD, 2000.
- [19] Y.-C. Liao, V. Yang, S.T. Thynell, in: V. Yang, T.B. Brill, W.Z. Ren (Eds.), *Solid Propellant Chemistry Combustion, and Motor Interior Ballistics*, in: *Progress in Astronautics and Aeronautics*, vol. 185, AIAA, Reston, VA, 2000, pp. 477–500.
- [20] E.S. Kim, Y.-C. Liao, V. Yang, *Combust. Flame* 131 (2002) 227–245.
- [21] T.A. Litzinger, Y.-J. Lee, C.-J. Tang, in: V. Yang, T.B. Brill, W.Z. Ren (Eds.), *Solid Propellant Chemistry Combustion, and Motor Interior Ballistics*, in: *Progress in Astronautics and Aeronautics*, vol. 185, AIAA, Reston, VA, 2000, pp. 355–379.
- [22] V. Yang, T.B. Brill, W.Z. Ren (Eds.), *Solid Propellant Chemistry Combustion, and Motor Interior Ballistics*, *Progress in Astronautics and Aeronautics*, vol. 185, AIAA, Reston, VA, 2000.
- [23] T. Parr, D. Hanson-Parr, *Combust. Flame* 127 (2001) 1895–1905.
- [24] T.P. Parr, D.M. Hanson-Parr, *Proc. 37th JANNAF Combustion Subcommittee Meeting*, vol. I, CPIA No. 701, Chemical Propulsion Information Agency, Columbia, MD, 2000, pp. 391–402.
- [25] S. Gordon, B.J. McBride, *Computer Program for Calculation of Complex Chemical Equilibrium Compositions and Applications*, NASA Reference Publication 1311, 1994.
- [26] D. Hanson-Parr, Personal communication, China Lake, CA, 2003.
- [27] K.V. Puduppakkam, PhD thesis, Department of Chemical Engineering, Brigham Young University, 2003.
- [28] T. Parr, D. Hanson-Parr, *Proc. 38th JANNAF Combustion Subcommittee Meeting*, vol. I, CPIA No. 712, Chemical Propulsion Information Agency, Columbia, MD, 2002, pp. 43–49.
- [29] D.M. Hanson-Parr, T.P. Parr, *J. Energ. Mater.* 17 (1999) 1–47.
- [30] T.B. Brill, *J. Propuls. Power* 11 (1995) 740–751.
- [31] B.D. Roos, T.B. Brill, *Combust. Flame* 128 (2002) 181–190.
- [32] Y. Oyumi, T.B. Brill, *Combust. Flame* 66 (1986) 9–16.
- [33] C.-Y. Lin, H.-T. Wang, M.C. Lin, C.F. Melius, *Int. J. Chem. Kinet.* 2 (2) (1990) 455–482.
- [34] G.S. Sysak, E.S. Kim, S.T. Thynell, *Proc. 35th JANNAF Combustion Meeting*, Tucson, AZ, December 7–11, 1998.

- [35] J.K. Chen, T.B. Brill, *Combust. Flame* 87 (1991) 157–168.
- [36] R.A. Fifer, in: K.K. Kuo, M. Summerfield (Eds.), *Fundamentals of Solid Propellant Combustion*, in: *Progress in Astronautics and Aeronautics*, vol. 90, 1984, pp. 177–219, Chap. 4.
- [37] G. Lengellé, A. Bizot, J. Durterque, J.F. Trubert, in: K.K. Kuo, M. Summerfield (Eds.), *Fundamentals of Solid Propellant Combustion*, in: *Progress in Astronautics and Aeronautics*, vol. 90, 1984, pp. 361–398, Chap. 7.
- [38] D. Chakraborty, M.C. Lin, in: V. Yang, T.B. Brill, W.Z. Ren (Eds.), *Solid Propellant Chemistry, Combustion, and Motor Interior Ballistics*, in: *Progress in Astronautics and Aeronautics*, vol. 185, AIAA, Reston, VA, 2000, pp. 33–71.
- [39] M. Frenklach, T. Bowman, G. Smith, B. Gardiner, GRI-MECH 3.0, downloaded from http://www.me.berkeley.edu/gri_mech/.
- [40] S.C. Li, F.A. Williams, S.B. Magolis, *Combust. Flame* 80 (1990) 329–349.
- [41] Yu.Ya. Maksimov, V.N. Apal'kova, O.V. Braverman, A.I. Solov'ev, *Russ. J. Phys. Chem.* 59 (1985) 201–204.
- [42] G. Edwards, *Trans. Faraday Soc.* 49 (1953) 152–154.
- [43] R.J. Kee, J.F. Grcar, M.D. Smooke, J.A. Miller, Sandia Report SAND85-8240, Sandia National Laboratories, Albuquerque, NM, 1985.
- [44] A. Zenin, *J. Propuls. Power* 11 (1995) 752–758.
- [45] A.I. Atwood, T.L. Boggs, P.O. Curran, T.P. Parr, D.M. Hanson-Parr, *J. Propuls. Power* 15 (1999) 740–752.
- [46] T. Parr, D.M. Hanson-Parr, Personal communication, China Lake, CA, 2003.
- [47] K. Puduppakkam, M.W. Beckstead, Proc. 39th JANNAF Combustion Subcommittee Meeting, CPIA Publ., Colorado Springs, December 2000.
- [48] D.R. Cruise, China Lake, NWC TP 6037, Nov. 1991.
- [49] V.G. Levich, *Dokl. Akad. Nauk SSSR* 109 (1956) 975.